

The observation of the South Atlantic Anomaly with the particle monitors onboard Insight-HXMT

The *Insight*-HXMT Collaboration

H.S. Zhao^{a,*}, C.Z. Liu^a, X.Q. Li^a, J.Y. Liao^a, J. Zhang^a, J.L. Qu^{a,b}, F.J. Lu^a, S.N. Zhang^{a,b}, L.M. Song^{a,b}, S. Zhang^a, T.P. Li^{a,b,c}, Y.P. Xu^{a,b}, X.L. Cao^a, Y. Chen^a

^a Key Laboratory of Particle Astrophysics, Institute of High Energy Physics, Chinese Academy of Sciences, Beijing 100049, China

^b University of Chinese Academy of Sciences, Chinese Academy of Sciences, Beijing 100049, China

^c Department of Astronomy, Tsinghua University, Beijing 100084, China

ARTICLE INFO

Article history:

Received 30 January 2020

Received in revised form 6 March 2020

Accepted 20 April 2020

Keywords:

South Atlantic Anomaly

Secular drift

Particle count

Insight-HXMT

ABSTRACT

The South Atlantic Anomaly (SAA) is a region of weakened geomagnetic field and in the previous studies, it shows a secular variation with time which is associated with the changing of the magnetic moment. This region also consists of large amounts of energetic charged particles and is danger to space vehicle and astronauts. Thus, it is essential to know the location and movement of the SAA. In this study, three particle monitors onboard Insight-HXMT are used to track the movement and location of the SAA from 2017 June 19 to 2019 June 19. Several particle flux maps are built to show the location of the SAA peak with time. In a grid of map, the particle count is determined by the maximum count rate and the averaged count rate, respectively. We find the results of both methods are consistent very well with each other in deriving the drift rate. The result shows the SAA peak moves westwards with an average drift rate of $0.43 \pm 0.01^\circ/\text{yr}$ in longitude and moves northwards with an average drift rate of $0.17 \pm 0.01^\circ/\text{yr}$ in latitude, and the drift rate is slightly larger than the result from IGRF 12 ($0.3^\circ/\text{yr}$) in longitude, but in latitude, the result of IGRF 12 have no obvious change with time.

© 2020 Elsevier B.V. All rights reserved.

1. Introduction

The Earth's magnetic field can be considered as a magnetic dipole with an axis that is offset from the Earth's center by about 500 km towards Southeast Asia and inclined by about 11° with respect to the Earth's rotational axis (Pinto et al., 1992). A numerical model called the International Geomagnetic Reference Field (IGRF) model (Finlay et al., 2010; Thébault et al., 2015) is used to calculate the Earth's magnetic field on or above Earth's surface. Its current version is IGRF12 with a definitive main field model for epoch 2010.0, a main field model for epoch 2015.0, and a linear annual predictive secular variation model for 2015.0–2020.0. The coefficients in the IGRF model are time-dependent and the time derivatives of these coefficients must be explicitly provided. Moreover, the Earth's magnetic field configuration determines the trapping and distribution of energetic ionized particles and the dis-

tribution of particle fluxes change in response to temporal changes in the geomagnetic field (Badhwar, 1997).

The South Atlantic Anomaly (SAA) is a region of weakened geomagnetic field, spans from east of Africa over the Atlantic Ocean to South America, and locates at a height of several hundred kilometers above the Earth's surface. Its peak in energetic particle flux is close to the geomagnetic field minimum. While the location of the minimum geomagnetic field within the SAA is also known to show a secular variation with time, associated with the changing of the magnetic moment, moving westward and northward (Anderson et al., 2018). The SAA also consists of large amounts of energetic charged particles, mainly electrons and protons, and these trapped ionized particles can produce electrical discharges from differential surface charging aboard satellites and cause damage to astronauts' DNA. Satellites will suffer much strong radiation when pass through the SAA, and this radiation damage and activation of the satellites materials would make the instruments unusable and produce 'glitches' or noise in astronomical data (Anderson et al., 2018). Thus, it is essential to know the drift speed of the SAA peak to improve the IGRF model, and the location of

* Corresponding author.

E-mail address: zhaohs@ihep.ac.cn (H.S. Zhao).

the SAA to protect space vehicle and astronauts. In the previous studies, a large number of measurements and investigations had been carried out over many years (e.g., Badhwar, 1997; Ginet et al., 2007; Grigoryan et al., 2008; Fürst et al., 2009; Casadio and Arino, 2011; Schaefer et al., 2016; Jones et al., 2017; Ye et al., 2017; Anderson et al., 2018). Badhwar (1997) used two data sets from Skylab (50° inclination × 438 km orbit) and Mir orbital station (51.65° inclination × 400 km orbit) to show that the drift rates of the SAA between 1973 and 1995 are $0.28 \pm 0.03^\circ/\text{W}$ and $0.08 \pm 0.03^\circ/\text{N}$ per year. Fürst et al. (2009) found that the SAA is drift westwards with an average drift rate of about $0.3^\circ/\text{yr}$ used the RXTE (23° inclination × 592 – 488 km orbit) 12 years of continuously data from 1996 to 2007. But RXTE can not cover the SAA completely and the result was dependent on fit shaping parameters. Jones et al. (2017) used SAMPEX (82° inclination)/LICA data to give a drift speed to be $0.20 \pm 0.04^\circ$ per year westward and $0.11 \pm 0.01^\circ$ per year northward from 1993 to 2011. SAMPEX altitude varied between 500 and 700 km and dropped sharply around 2000 by about 200 km. Schaefer et al. (2016) used DMSP (99° inclination × 840 km orbit) F16/SSUSI data to show an average of $0.36 \pm 0.06^\circ/\text{W}/\text{yr}$ and $0.16 \pm 0.09^\circ/\text{N}/\text{yr}$. And Anderson et al. (2018) used DMSP/SSJ and Proba-V/EPT to get a $0.28^\circ/\text{W}/\text{yr}$ and $0.06^\circ/\text{N}/\text{yr}$ from 1988 to 2015. However, the SSUSI and SSJ are in different locations on DMSP F16 and do experience a different population of particles, and different SSJ instruments from DMSP F8 – F18 satellites have different responses to charged particles. These facts can lead to different locations of the SAA. In a word, the drift values of the SAA appear to be spread over an abnormally large range. The minimum drift rate reported is $0.17^\circ/\text{yr}$ W and $0.08^\circ/\text{yr}$ N, and the maximum drift rate reported is $0.66^\circ/\text{yr}$ W and $0.22^\circ/\text{yr}$ N (Anderson et al., 2018).

In our study, we use data obtained by three particle monitors on the Hard X-ray Modulation Telescope satellite from 2017 June 19 to 2019 June 19 to track the movement and the location of the SAA.

2. Instrumentation and data acquisition

The Hard X-ray Modulation Telescope (dubbed as Insight-HXMT) satellite (Zhang et al., 2020) was launched on 2017 June 15 in China with a quasi-spherical orbit at an altitude of 550 km. With an inclination of 43° and an orbital period of 90 min, the satellite passes fully through the SAA about 8 times per day on average. There are three main payloads onboard Insight-HXMT, the High Energy X-ray telescope (HE) (Liu et al., 2020), the Medium Energy X-ray telescope (ME) (Cao et al., 2020) and the Low energy X-ray telescope (LE) (Chen et al., 2020), to sum up a broad energy band coverage of 1 – 250 keV. An auxiliary payload that carries three identical particle monitors (PM) (Lu et al., 2020), is designed to monitor the flux of high energy charged particles. Once the count rate of particle monitors exceeds the threshold set by the ground, especially when the satellite passes through the SAA region, the Insight-HXMT payloads will reduce the high voltages of main payloads to protect themselves from damage.

The three particle monitors are integrated on the same supporting structure as the main payloads. One particle monitor numbered 0 (PM0) is put at the side of HE, while other two numbered 1 (PM1) and 2 (PM2) are installed on the opposite direction of PM0 and also put beside HE. Each particle monitor consists of a small plastic scintillator and a photomultiplier tube (PMT), and the plastic scintillator is machined into a cylinder with both a diameter and a height of 10 mm, while PMT is used to read out the scintillation light. The surrounding of scintillator is an aluminum shell, and this shell can block low-energy gamma-rays and become transparent to high-energy gamma-rays. According to simulation, the particle monitor is sensitive to electrons with energy higher than

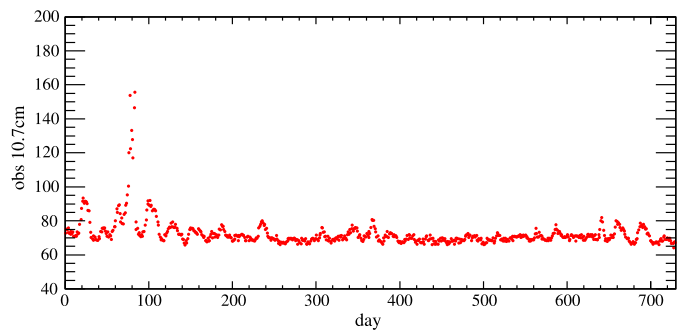


Fig. 1. The averaged observations of $F_{10.7}$ cm flux vary with time during the time between 2017 June 19 and 2019 June 19. The begin time is 2017 June 19.

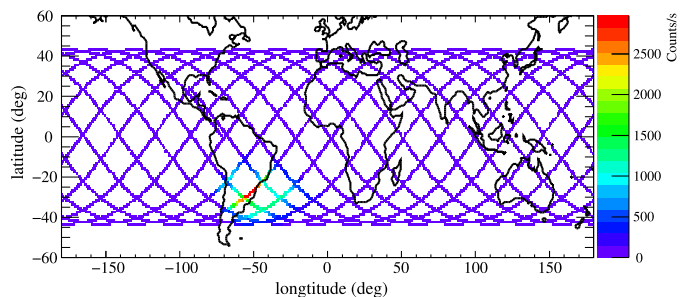


Fig. 2. One day orbit and the count rate change of particle flux for PM2 of Insight-HXMT on 2018 August 22. (For interpretation of the colors in the figure(s), the reader is referred to the web version of this article.)

1 MeV and protons with energy higher than 20 MeV. The incident charged particles can hit the PM from frontside within 2π solid angle and cause signal in plastic scintillator. If the amplitude of signal in PMT is higher than the threshold, the hit will be recorded. Thus, the count rates of the three PMs will be recorded every second but without energy resolution. Due to this quick readout mode, the data obtained by PMs will not be saturated. The constituents of PMs are carbon and hydrogen, and these elements are to the least degree subjected to activation.

The Insight-HXMT data in this study comes from the time period of 2017 June 19 to 2019 June 19. Corresponding to this period, the averaged solar 10.7 cm radio flux (the data is downloaded from the Space Weather Prediction Center) is shown in Fig. 1. And in this period, most of the time solar is in lower activity. There are several days around 2017 September 10, when solar was in higher activity, while Insight-HXMT was shut down to protect the payloads and no data was obtained by PMs. Beyond this, some time intervals around this period are removed in this study. Some data with bad quality, which may be due to data transmission error or data processing error, are also removed. There is no obvious evidence count rate excess, when the satellite is in time of gamma-ray bursts or solar flare bursts.

In this period, the orbital altitude of Insight-HXMT consistently varied between 530 km and 560 km, and the averaged altitude was 545.5 km and decreased by 1 km/yr.

3. Methodology and results

3.1. Methodology

The count rates of PMs are related to attitude and their location with respect to satellite. Fig. 2 shows one day orbit and the change of count rate for PM2 on 2018 August 22, and the rates are different when the satellite passes the same region with different attitudes. There are only several events per second at most area

Table 1

The start and stop time of data segments (the format of date is 'yyyymmdd'). The different durations for these segments are due to the orbital coverage and orbital coverage of Insight-HXMT is not uniform.

Bin number	1	2	3	4	5	6	7	8
Time bins	20170619 –20170819	20170819 –20171119	20171119 –20180719	20180719 –20181019	20181019 –20181219	20181219 –20190219	20190219 –20190419	20190419 –20190619
Duration days	61	92	242	92	61	62	59	61

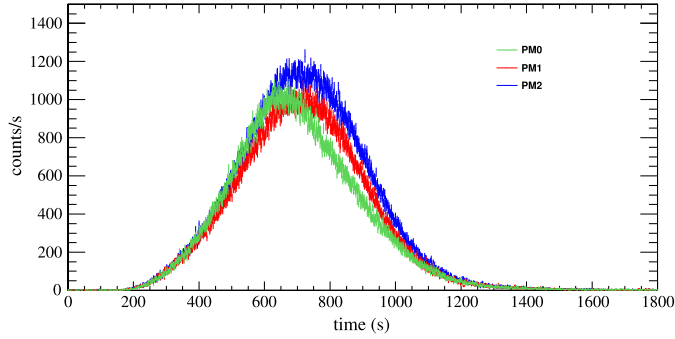


Fig. 3. The count rate values of three particle monitors versus time of Insight-HXMT for a short time interval.

outside the SAA, while there are thousands of events per second in the area of the SAA.

Fig. 3 shows the evolution of the count rates of the three particle monitors versus time for a short time interval. The time corresponding to the maximum of count rates for three PMs is different, especially for the time of PM0. On reason for the difference is that they are in different locations and do experience a different direction of particles. The largest time-lag is about 40 s, which corresponds to 2.4° in longitude and $0.4 - 0.8^\circ$ in latitude. But after each SAA passage, the count rates decrease rapidly, which indicates that the surrounding materials and PM constituents (mainly carbon and oxygen) have no obvious activation by space environment.

In order to study the location and movement of the SAA, a particle flux map is determined with a time resolution of several months (e.g., 2 months) and a spatial resolution of 0.5° in longitude and 0.5° in latitude (each a $0.5^\circ \times 0.5^\circ$ is called a grid).

For a grid, the satellite will experience many times with different attitudes and hence, the maximum count rate in accumulated observational data has a great probability to correspond to the direction of maximum flux. Thus, there are two methods to determine the particle count of a grid at a given time bin: (1) method A, the maximum count rate from the accumulated observational data is taken as this grid's particle count; (2) method B, the averaged count rate is taken as particle count. Then, the count rate values as a function of longitude/latitude are summed up over latitude/longitude bins in the selected region. This distribution of the count rates with longitude/latitude can be described using Weibull function (Weibull, 1951), with the peak describing the position of the SAA peak. The Weibull function is an asymmetric function and defined by

$$y(x; A, k, \lambda, \theta) = \begin{cases} A \cdot \frac{k}{\lambda} \cdot \left(\frac{x-\theta}{\lambda}\right)^{k-1} \cdot \exp\left(-\left(\frac{x-\theta}{\lambda}\right)^k\right) & x \geq \theta \\ 0 & x \leq \theta \end{cases} \quad (1)$$

Here, x is the geographic longitude/latitude; A is the normalization, λ is the scale parameter, θ is the shift parameter, and k is the shape parameter of the Weibull function. The position of the maximum of the Weibull function, \hat{x} , is given by

$$\bar{x} = \lambda \cdot \left(\frac{k-1}{k}\right)^{\frac{1}{k}} + \theta \quad (2)$$

The data of three particle monitors are used independently to build the particle flux map. Fig. 4 shows the normalized particle count rate values of three particle monitors versus longitude (left) and latitude (right) for the time from 2017 June 19 to 2017 August 19, and the data are fitted by Weibull function (red line). Row 1, 2 and 3 show the data of PM0, PM1 and PM2, respectively, and column 1 and 3 show the data of method A, while column 2 and 4 show the data of method B.

To determine the longitudinal location of the SAA, the data are accumulated from -100°W to 30°E along the longitude and from 0° to -43°S along latitude, while to determine the latitudinal location, the data are accumulated from -180°W to 80°E along longitude and from 0° to -43°S along latitude. Enlargement and reduction of these ranges do not affect the determination of the location of the SAA. The fit range is about from -68°W to -32°W along longitude and from -35°S to -20°S along latitude. The error from the range is less than 0.02° for both latitude and longitude.

To determine the drift of the SAA peak, the data over the 2-year period are divided into 8 segments, each with a good orbital coverage. Some segments have long duration since the Insight-HXMT orbital coverage is not uniform. Table 1 shows the start and stop time of these data segments.

3.2. Movement of the SAA

The particle count rates of each PM obtained by method A and B as a function of longitude/latitude for each data segment are fitted with the Weibull function and Fig. 5 shows the locations (points) of the SAA peak for 8 segments of each PM. As shown in Fig. 5, there is a clear offset between the SAA peak locations of both methods. The identified longitude values of method A for the SAA peak are slightly farther southern than those of method B by about 0.4° , while the identified of latitude values of method A are slightly farther northern than those of method B by about 0.5° . The locations of three PMs for method A show similar trends, while the locations of PM1 and PM2 show similar trends, but different from the locations of PM0. The comparison of locations of three PMs for each data segment shows that there are some differences among them. These differences among PMs may be due to the different surrounding materials, the triggered threshold energy, response to charged particles, and poor attitudinal coverage. The surrounding materials, which can block and scatter the incident charged particles are different for the three PMs, especially for PM0, which is closer to a star sensor. Although the triggered threshold for electrons is designed to be about 1 MeV and that for proton is about 20 MeV, they may be different for three PMs. According to simulation (Lu et al., 2020), the threshold has a relationship to the temperature and the working temperature on board Insight-HXMT for three PMs are different. While the data of all the 2 years are fitted by Weibull function and the identified positions of the SAA peak are shown in Table 2. The differences of the identified peak among three PMs are less than the ones of the previous results. So, one reason for the difference may be due to poor attitudinal coverage.

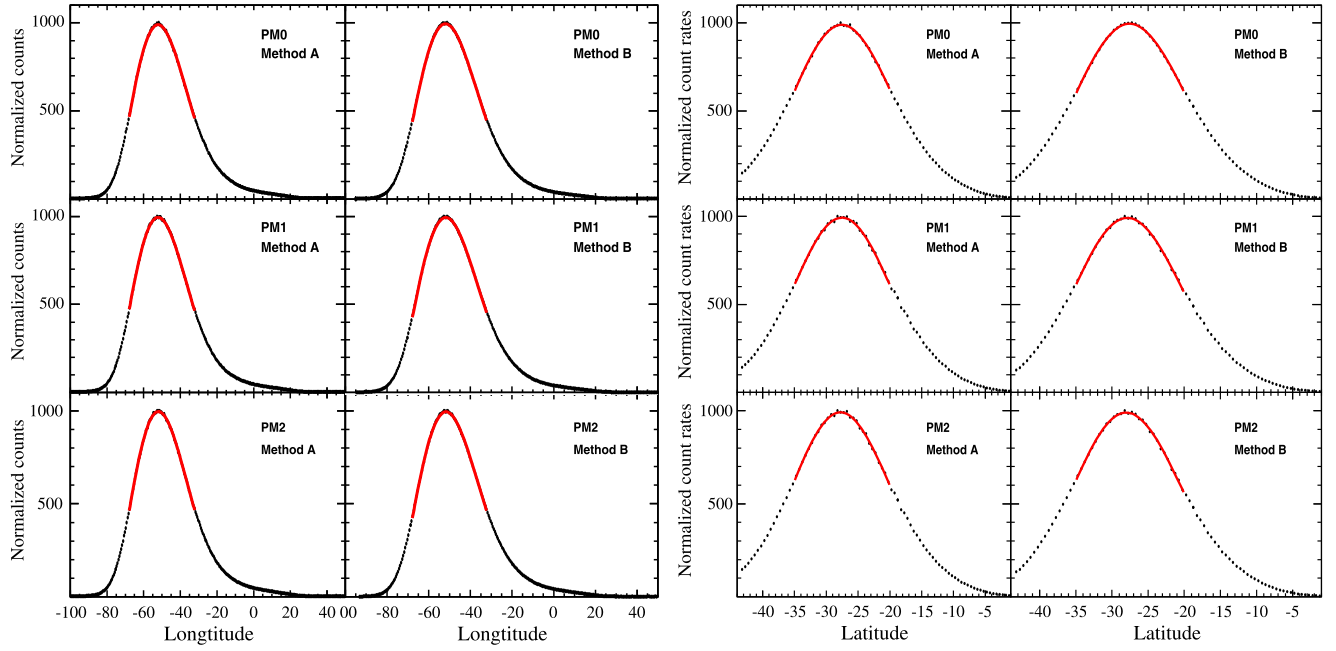


Fig. 4. Normalized particle count rate values versus longitude/latitude from 2017 June 19 to 2017 August 19 are fitted by Weibull function for three PMs, respectively. The fitted line is in red. Row 1, 2 and 3 show the data of PM0, PM1 and PM2, respectively, and column 1 and 3 show the data obtained by method A, while column 2 and 4 show the data obtained by method B.

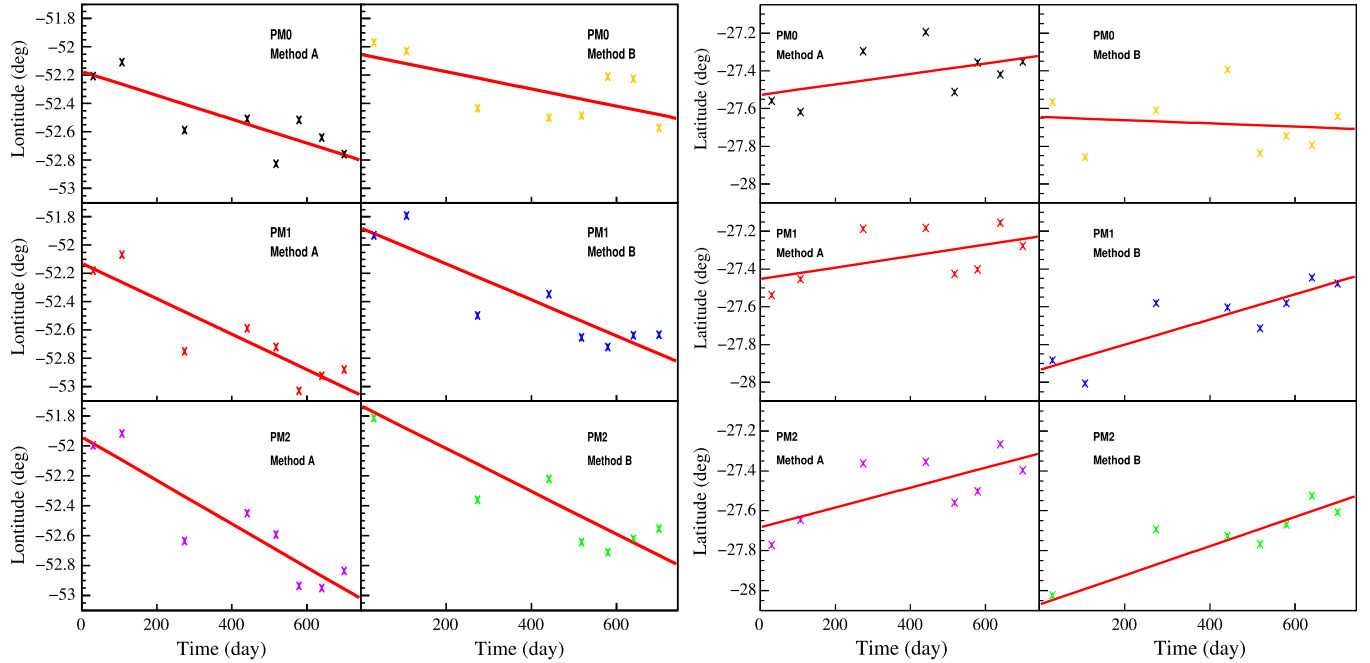


Fig. 5. The identified longitude and latitude values of the SAA peak. The lines are linear fits to the data for the two method and for the three particle monitors.

Table 2

The identified position of the SAA peak from 2017 June 19 to 2019 June 19.

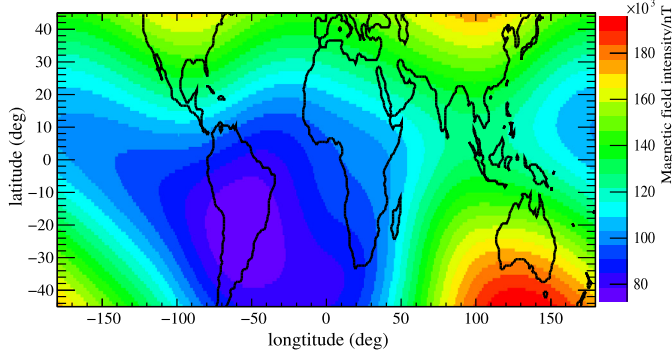
Methon	PM	Longitude position ($^{\circ}$)	Latitude position ($^{\circ}$)
Method A	0	-52.71 ± 0.02	-27.14 ± 0.02
	1	-52.80 ± 0.02	-27.17 ± 0.02
	2	-52.72 ± 0.02	-27.31 ± 0.02
Method B	0	-52.27 ± 0.02	-27.69 ± 0.02
	1	-52.38 ± 0.02	-27.66 ± 0.02
	2	-52.30 ± 0.02	-27.77 ± 0.02
Method A	ALL	-52.74 ± 0.01	-27.20 ± 0.01
Method B	ALL	-52.32 ± 0.01	-27.71 ± 0.01

The identified longitudes and latitudes of the SAA peak versus time for both method A and B are fitted with a linear fit and the fitted results indicate the drift rate of the SAA peak. Table 3 shows the linear fit results and the error comes from the fitted error (if the error is less than 0.01° , 0.01° will be taken as error value). In Fig. 5, the lines show linear fits to the identified longitudes and latitudes, and the movement is relatively linear. For each method, the longitudes/latitudes of each data segment of three PMs are averaged and these averaged positions are still fitted with a linear fit. The result of the fit is $-0.45 \pm 0.01^{\circ}/\text{yr}$ in longitude and $0.17 \pm 0.01^{\circ}/\text{yr}$ in latitude for method A, while for method B, the result of the fit is $-0.42 \pm 0.01^{\circ}/\text{yr}$ in longitude

Table 3

The drift rate in longitude and latitude.

Method	PM	Longitude drift ($^{\circ}/\text{yr}$)	Latitude drift ($^{\circ}/\text{yr}$)
Method A	0	-0.31 ± 0.01	0.10 ± 0.01
	1	-0.46 ± 0.01	0.11 ± 0.01
	2	-0.53 ± 0.01	0.18 ± 0.01
Method B	0	-0.22 ± 0.01	-0.03 ± 0.01
	1	-0.46 ± 0.01	0.24 ± 0.01
	2	-0.52 ± 0.01	0.27 ± 0.01
Method A	ALL	-0.45 ± 0.01	0.17 ± 0.01
Method B	ALL	-0.42 ± 0.01	0.17 ± 0.01
Combined AB	ALL	-0.43 ± 0.01	0.17 ± 0.01

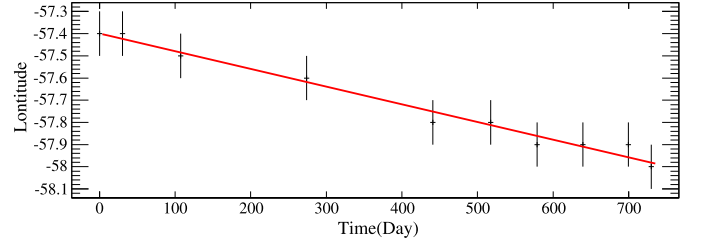
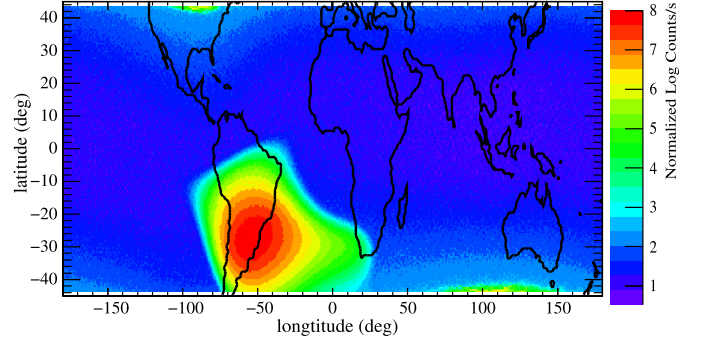
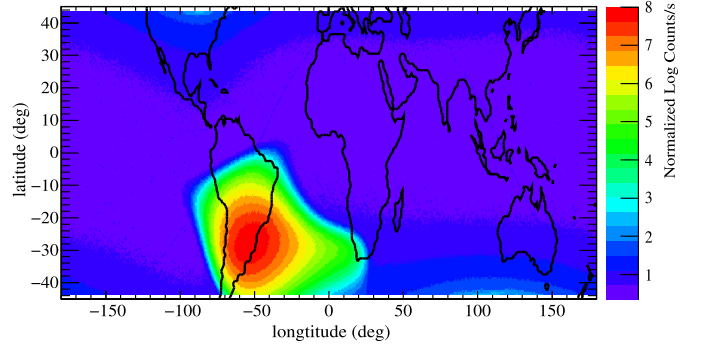
**Fig. 6.** The intensity of the magnetic field in 20180619 from IGRF 12.

and $0.17 \pm 0.01^{\circ}/\text{yr}$ in latitude. The drift rates of two methods are consistent with each other very well. At last, the results of both methods are combined and the combined result is that the SAA moves $-0.43 \pm 0.01^{\circ}$ westward per year and $0.17 \pm 0.01^{\circ}$ northward. In the previous studies, there is a wide range of published results on the SAA movement and the result of this work is within the range of published values. However, the drift rates (in both longitude and latitude) of this work are larger than the results of Badhwar (1997), Fürst et al. (2009), Jones et al. (2017) and Anderson et al. (2018). Table 4 shows the comparison of the SAA drift rates among these results. But the data obtained with these works were taken as different altitude, different energetic particle and different energy band.

The derived observational result for SAA movement is also compared to the IGRF 12 model. Fig. 6 shows the intensity of the magnetic field in 2018 June 19 from IGRF 12. Similarly, the maps of magnetic field intensity are built at the center time of each bin (shown in Table 1) with a spatial resolution of $0.1^{\circ} \times 0.1^{\circ}$ and an altitude of 550 km. The location of minimum intensity is searched in a region of -80°W to -35°W in longitude, -35°S to -10°S in latitude, with a step of 0.1° in both directions. Fig. 7 shows the change from 2017 June 19 to 2019 June 19 in longitude and the drift rate is fitted to a straight line, which denotes a drift rate of $0.3^{\circ}/\text{yr}$ and hence the SAA moves westwards. But there is no obvious change with time in latitude (the value is around -22.2°).

3.3. Mapping the SAA

Table 2 shows the Weibull fit results of the SAA peak and the results of each PM are consistent very well with each other. But there are some differences for the results of the SAA peak between the both methods. Thus, in order to study the shape and location of the SAA, the method A and method B are used to build the particle flux map, respectively. The maps of three PMs are combined to build an averaged map. For both methods, the peak count rate is normalized to 3000 cnt/s. Figs. 8 and 9 show the maps of the particle count of the three PMs obtained by the method A and B from

**Fig. 7.** The longitude location of the minimum in the magnetic field from IGRF 12. The read lines are linear fits to the data and the drift rate is $0.3^{\circ}/\text{yr}$.**Fig. 8.** Geographic map of the maximum count rate of the three particle monitors of Insight-HXMT from 2017 June 19 to 2019 June 19.**Fig. 9.** Geographic map of the averaged count rate of the three particle monitors of Insight-HXMT from 2017 June 19 to 2019 June 19.

2017 June 19 to 2019 June 19. The identified values of the SAA peak for method A and B are $-52.74 \pm 0.01^{\circ}\text{W}$, $-27.20 \pm 0.01^{\circ}\text{S}$ (method A), and $-52.32 \pm 0.01^{\circ}\text{W}$, $-27.71 \pm 0.01^{\circ}\text{S}$ (method B), respectively. For IGRF 12, the position of minimum in the magnetic field at 2018 June 19 is about -57.7°W and -22.2°S .

In each grid, the particle count rate of method A is divided by the one of method B, and this means the maximum particle count rate when the satellite passes through this region is compared to the averaged particle count rate. Fig. 10 shows the map of such a ratio distribution. The maximum ratio is always located at higher latitude region, while the minimum ratio is in the SAA region (near -51°W and -31°S). The ratios in the SAA region are close to 1 and this indicates that the particle fluxes in the SAA region are similar in all directions. This is the reason why the results of two method A and B are in good agreement.

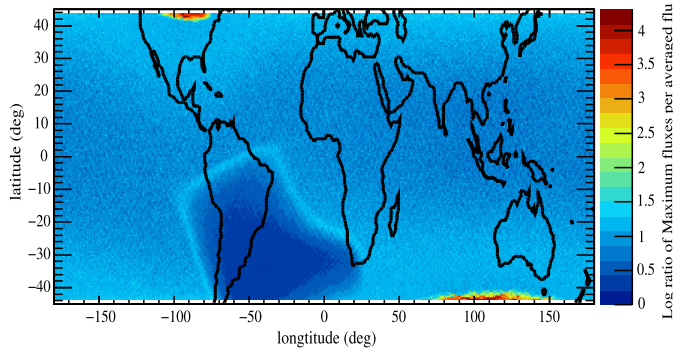
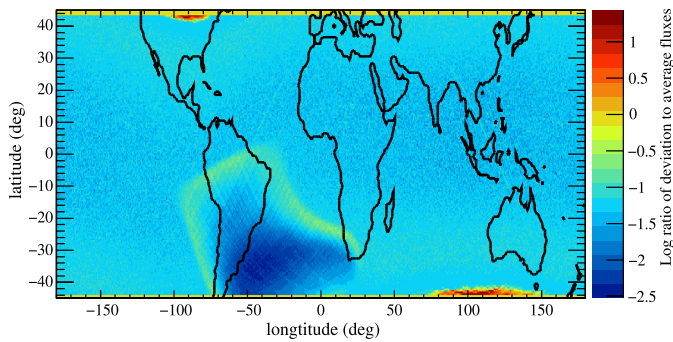
We also compare the deviation to the averaged particle count rate (σ/\bar{f}) for method B in each grid, and the definition of deviation is given by:

$$\sigma = \left(\frac{1}{N-1} \left(\sum_{i=1}^N (f_i - \bar{f})^2 \right) \right)^{\frac{1}{2}} \quad (3)$$

Table 4

Comparison of the SAA drift rates between some previous studies and this work.

Years	Altitude (km)	Longitude drift ($^{\circ}/\text{yr}$)	Latitude drift ($^{\circ}/\text{yr}$)	reference
1973–1995	438 and 400	0.28 ± 0.03	0.08 ± 0.03	Badhwar (1997)
2000–2006	400–1710	0.43 ± 0.13		Ginet et al. (2007)
1996–2007	592–488	0.3		Fürst et al. (2009)
2004–2011	850	0.36 ± 0.06	0.16 ± 0.09	Schaefer et al. (2016)
1993–2011	500–700	0.20 ± 0.04	0.11 ± 0.01	Jones et al. (2017)
1998–2015	840	0.28	0.06	Anderson et al. (2018)
2016–2019	550	0.43 ± 0.01	0.17 ± 0.01	this work

**Fig. 10.** The ratios of maximum fluxes per average flux.**Fig. 11.** The ratios of deviation to average fluxes.

where f_i is the i th ($i = 1 \dots N$) particle count rate, \bar{f} means the averaged particle count rate, and N is the total number of data point number. Fig. 11 shows the ratios of deviation to average fluxes. The minimum deviation also in the SAA region near -50°W and -32°S . Both Figs. 10 and 11 are consistent with each other very well. We also note that at the edge of the SAA, the particle fluxes vary greatly in different directions.

4. Summary

The location of the SAA peak depends on the particle distribution in the radiation belts, the energy of the observed particles, and the altitude of the observations (Anderson et al., 2018). In this study, we have used three particle monitors aboard Insight-HXMT to track the movement and location of the SAA from 2017 June 19 to 2019 June 19. In the last two years since launch, the orbital altitude of Insight-HXMT kept around 550 km and only decreased by 1 km/yr mainly due to the atmospheric drag. And during this period, the solar 10.7 cm radio flux was almost constant and kept at a low level. The particle flux is inversely correlated with the 10.7 cm radio flux, and this inverse-correlation is due to heating of the upper atmosphere. The heating leads to a higher neutral density in the altitude region of the SAA and consequently to a higher absorption and deflection of trapped particles, which results in a lower particle flux compared to times of lower solar activity (Fürst

et al., 2009). Thus, this two-year 10.7 cm radio flux provides a constant space environment to monitor the movement of the SAA. More interestingly, the Sun will be still in lower activity in 2020.

To study the location of the SAA, the averaged count rate method and the maximum count rate method are used to build the maps. The averaged count rate method was widely adopted previously and gives the peak of the SAA of $-52.32 \pm 0.01^{\circ}\text{W}$, $-27.71 \pm 0.01^{\circ}\text{S}$, while the maximum count rate method gives the peak of the SAA of $-52.74 \pm 0.01^{\circ}\text{W}$, $-27.20 \pm 0.01^{\circ}\text{S}$. The shapes and drift rates between both methods are consistent with each other. We found that the particle fluxes in all directions are consistent with each other in the SAA region, but vary greatly at the edge of the SAA. A linear fit is used to localize the position of the SAA peak and this Insight-HXMT data confirm earlier measurements of a westward drift of the SAA with a rate of $0.43 \pm 0.01^{\circ}$, a northward drift with a rate of $0.17 \pm 0.01^{\circ}$. But, from Fig. 5, the identified positions show that the drift rates is not constant. The drift rates of this work are also compared to the IGRF 12 model and it is slightly larger than the result from IGRF 12 ($0.3^{\circ}/\text{yr}$) in longitude, but in latitude, the result of IGRF 12 have no obvious change with time.

Declaration of competing interest

The authors declare that they have no known competing financial interests or personal relationships that could have appeared to influence the work reported in this paper.

Acknowledgments

This work made use of the data from the *Insight-HXMT* mission, a project funded by China National Space Administration (CNSA) and the Chinese Academy of Sciences (CAS). The authors thank supports from the National Program on Key Research and Development Project (Grant No. 2016YFA0400802) and the National Natural Science Foundation of China under Grants No. U1938102, U1838202, U1838201, 11503029, and 11403026.

References

- Anderson, P.C., Rich, F.J., Borisov, Stanislav, 2018. Mapping the South Atlantic Anomaly continuously over 27 years. *J. Atmos. Terr. Phys.* 177, 237–246.
- Badhwar, G., 1997. Drift rate of the South Atlantic Anomaly. *J. Geophys. Res.* 102, 2343–2349.
- Cao, X.L., Jiang, W.C., Meng, B., Zhang, W.C., Luo, T., Yang, S., et al., 2020. The Medium Energy (ME) X-ray telescope onboard the Insight-HXMT astronomy satellite. *Sci. China, Phys. Mech. Astron.* 63 (4), 249504. [arXiv:1910.04451](https://arxiv.org/abs/1910.04451).
- Casadio, S., Arino, O., 2011. Monitoring the South Atlantic Anomaly using ATSR instrument series. *Adv. Space Res.* 48 (6), 1056–1066. <https://doi.org/10.1016/j.asr.2011.05.014>.
- Chen, Y., Cui, W.W., Li, W., Wang, J., Xu, Y.P., Lu, F.J., et al., 2020. The Low Energy X-ray telescope (LE) onboard the Insight-HXMT astronomy satellite. *Sci. China, Phys. Mech. Astron.* 63 (4), 249505. <https://doi.org/10.1007/s11433-019-1469-5>.
- Finlay, C.C., et al., 2010. International geomagnetic reference field: the eleventh generation. *Geophys. J. Int.* 183, 1216–1230.
- Fürst, F., et al., 2009. Temporal variations of strength and location of the South Atlantic Anomaly as measured by RXT. *Earth Planet. Sci. Lett.* 281, 125–133.

- Ginet, G.P., Madden, D., Dichter, B.K., Brautigam, D.H., 2007. Energetic Proton Maps for the South Atlantic Anomaly. Paper presented at IEEE Radiation Effects Data Workshop, Waikiki, Hawaii, 23–27 Jul.
- Grigoryan, O.R., Romashova, V.V., Petrov, A.N., 2008. SAA drift: experimental results. *Adv. Space Res.* 41, 76–80.
- Jones, A.D., Baker, D.N., et al., 2017. SAMPEX observations of the South Atlantic anomaly secular drift during solar cycles 22–24. *Space Weather* 15 (1), 44–52.
- Liu, C.Z., Zhang, Y.F., Li, X.F., Lu, X.F., Chang, Z., Zhang, A.M., et al., 2020. The high energy X-ray telescope (HE) onboard the Insight-HXMT astronomy satellite. *Sci. China, Phys. Mech. Astron.* 63 (4), 249503. [arXiv:1910.04955](https://arxiv.org/abs/1910.04955).
- Lu, X.F., Liu, C.Z., et al., 2020. Design and calibration of high energy particle monitor on board HXMT. <https://doi.org/10.1016/j.jheap.2020.02.006>.
- Pinto Jr., O., Gonzalez, W.D., Pinto, I.R.C.A., et al., 1992. The South Atlantic magnetic anomaly. *J. Atmos. Terr. Phys.* 54, 1129.
- Schaefer, R.K., Raxton, IJ, et al., 2016. Observation and modeling of the South Atlantic Anomaly in low Earth orbit using photometric instrument data. *Space Weather* 14, 330–342.
- Thébault, Erwan, Finlay, Christopher, et al., 2015. International geomagnetic reference field: the 12th generation. *Earth Planets Space* 67, 79.
- Weibull, W., 1951. A statistical distribution function of wide applicability. *J. Appl. Math.* 18, 293–297.
- Ye, Y., Zou, H., Zong, Q., Chen, H., Wang, Y., Yu, X., Shi, W., 2017. The secular variation of the center of geomagnetic South Atlantic Anomaly and its effect on the distribution of inner radiation belt particles. *Space Weather* 15, 1548–1558. <https://doi.org/10.1002/2017SW001687>.
- Zhang, S.N., Li, T.P., Lu, F.J., Song, L.M., Xu, Y.P., Liu, C.Z., et al., 2020. Overview to the hard X-ray modulation telescope (Insight-HXMT) satellite. *Sci. China, Phys. Mech. Astron.* 63 (4), 249502. <https://doi.org/10.1007/s11433-019-1432-6>.